The Identification and Tracking of Volcanic Ash using the Meteosat Second Generation (MSG) Spinning Enhanced Visible and Infra-Red Imager (SEVIRI)

Aaron R. Naeger[1] and Sundar A. Christopher[1,2]

[1]Earth System Science Center, UAHuntsville, 320 Sparkman Drive
Huntsville, AL, 35805

[2]Department of Atmospheric Sciences, UAHuntsville, 320 Sparkman Drive
Huntsville, AL 35805

Submitted to:
Atmospheric Measurement Techniques
May 2013

Abstract

In this paper, we develop an algorithm based on combining spectral, spatial, and temporal thresholds from the geostationary Spinning Enhanced Visible and InfraRed Imager (SEVIRI) daytime measurements to identify and track different aerosol types, primarily volcanic ash. Contemporary methods typically do not use temporal information to identify ash. We focus not only on the identification and tracking of volcanic ash during the Eyjafjallajökull volcanic eruption period beginning 14 April to **17 May 2010** but a pixel level classification method for separating various classes in the SEVIRI images. Three case studies on **13 May**, 16 May, and 17 May are analyzed in extensive detail with other satellite data including the Moderate Resolution Imaging Spectroradiometer (MODIS), Multi-angle Imaging Spectroradiometer (MISR), and Facility for Airborne Atmospheric Measurements (FAAM) BAe146 aircraft data to verify the aerosol spatial distribution maps generated by the SEVIRI algorithm. Our results indicate that the SEVIRI algorithm is able to track volcanic ash **when the solar zenith angle is lower than about 65°.** Furthermore, the BAe146 aircraft data shows that the SEVIRI algorithm detects nearly all ash regions when AOD > 0.2. However, the algorithm has higher uncertainties when AOD is < 0.1 over water and AOD < 0.2 over land. The ash spatial distributions provided by this algorithm can be used as a critical input and validation for atmospheric dispersion models simulated by Volcanic Ash Advisory Centers (VAACs). Identifying volcanic ash is an important first step before quantitative retrievals of ash concentration can be made.

1. Introduction

The Eyjafjallajökull volcano located on the southern coast of Iceland (63.6°N, 19.6°W) began emitting ash into the atmosphere on 14 April 2010. Although only a mid-size eruption (**Gudmundsson et al., 2013**), the volcano had a tremendous impact on air traffic as the strong atmospheric winds transported the ash southeasterly towards Europe (Ansmann et al., 2010a). By 16 April 2010, an ash plume was observed across Central Europe by Aerosol Robotic Network (AERONET) Sun photometers and ground based lidars (Ansmann et al., 2010b). The presence of ash caused nearly a week-long stoppage in air travel over many parts of Europe since **volcanic ash can have damaging effects on commercial airplanes** (Casadevall, 1992). Flight cancellations that occurred over the ensuing week proved extremely costly to the airline industry as monetary losses were over 1 billion U.S. dollars **(Christopher et al., 2012).** Therefore, it is critical that we accurately track volcanic ash during an eruption period.

To track the spatial distribution of volcanic ash, satellite remote sensing is important as the spatial distribution of ash varies strongly especially after an eruption. Ground based stations are inadequate for understanding the spatial distribution as they only provide point measurements. Satellites are also an important tool for verifying models that predict ash concentrations and spatial distributions (Millington et al., 2012). These models are usually high resolution dispersion models that predict height dependent ash concentrations used by Volcanic Ash Advisory Centers (VAACs). Although polar orbiting satellites such as the Moderate Resolution Imaging Spectroradiometer (MODIS) can provide high spatial resolution of volcanic ash plumes (Sigmundsson et al., 2010), their temporal resolution is insufficient to track ash plumes being transported long distances over relatively short time scales. Thus, geostationary satellite sensors such as the Spinning Enhanced Visible and InfraRed Imager (SEVIRI) are critical for assessing the spatial distributions of ash due to their high temporal resolutions (Prata and Kerkmann, 2007, Christopher, et al., 2012).

Ultimately it is important to know the vertical distribution of ash concentrations before important decisions can be made regarding commercial flights during eruptions. However the first task is to detect the volcanic ash on a pixel-by-pixel basis. The first limitation to note is the SEVIRI cannot detect ash below **thick** clouds which is a common issue for passive satellite data sets that operate in the visible to the infrared part of the electromagnetic spectrum. However the repeated temporal information and the large spatial coverage make SEVIRI an excellent tool **for understanding the spatial distribution of volcanic ash over large areas.** One common method is to simply assign separate channels to the red, green, and blue and visually **examine** the ash by looking for certain colors. This is often problematic since clouds can be confused as ash and not all aerosols appear to have the same color; and therefore, it is important to develop an algorithm that separates an image into various classes, such as cloud and aerosol, for further studies that may involve calculation of ash concentrations.

Prata (1989) presented a very commonly used technique that exploits the brightness temperature difference (BTD) between the 11 and 12 μm channels (BTD 11-12). The limitations with this simple technique are well known and discussed in Prata et al. (2001) where one major limitation is that high water vapor amounts can mask the negative BTD signal which the technique relies on ash detection. Pergola et al. (2004) developed a more sophisticated ash detection technique that compares a measured satellite signal to a reference field computed from long-term historical records. In particular, they use three channels centered at approximately 3.75, 11.0, and 12.0 μm from the Advanced Very High Resolution (AVHRR) to compute the reference fields and they show that this Robust AVHRR Technique (RAT) is more accurate in detecting volcanic ash than the simple BTD technique presented in Prata (1989). However, this approach requires multiple years of data over a region to compute the reference fields. Pavolonis et al. (2006) developed a four channel ash detection algorithm that utilizes the 0.65, 3.75, 11.0, and 12.0 μm channels and does not rely on a reference field but instead uses spectral tests and a spatial filtering routine. They showed that this four channel algorithm is much better at detecting volcanic ash regions compared to the BTD approach with less false detections. We take a different approach by developing an algorithm using SEVIRI measurements that exploits temporal thresholds along with spectral and spatial thresholds to classify each pixel into various classes (e.g. cloud, land, and aerosol). This algorithm uses seven different SEVIRI channels to produce detailed spatial distribution maps of cloud and aerosol.

Although the SEVIRI instrument is not equipped with near ultraviolet (UV) channels, it is important to note the ability of the near-UV channels in detecting volcanic ash. Torres et al. (1998) used the near-UV channels of 340 and 380 nm from the Total Ozone Mapping Spectrometer (TOMS) instrument to detect volcanic ash, and they found that these two channels have great success in detecting ash over snow/ice or above clouds. This is an important advantage of using the near-UV channels as detection techniques using channels from the visible to infrared spectrums, such as the RAT and our SEVIRI algorithm, do not possess the same capability of detecting ash over snow/ice or above clouds (Pergola et al., 2004). In addition, Krotkov et al. (1999) showed that the near-UV channels of the TOMS instrument can detect the optically opaque, very fresh ash which is often missed by the visible and infrared techniques.

This study tracks the ash plumes emitted from the Eyjafjallajökull volcano from its initial eruption on 14 April until the end of the eruption period on 23 May using the high temporal resolution measurements of SEVIRI onboard the Meteosat Second Generation (MSG-2) satellite. Since we use the visible along with the infrared channels of SEVIRI, the algorithm developed in this study can only track the ash plumes during the daylight periods for volcanic ash in cloud-free conditions. We present results from the SEVIRI algorithm throughout the eruption period but place special emphasis on six days in May 2010 when the Facility for Airborne Atmospheric Measurements (FAAM) BAe146 research aircraft measurements was available (Johnson et al., 2012). We use the FAAM BAe146 aircraft measurements as validation for the SEVIRI algorithm developed in this study. Other sources of verification data used in this study to assess the spatial distribution of the aerosols detected by the SEVIRI algorithm include the MODIS,and the Multi-angle Imaging SpectroRadiometer (MISR).

2. Data

The goal of the paper is to develop a pixel level algorithm from SEVIRI reflectance and temperature measurements using temporal threshold tests along with spatial and spectral threshold tests. It is important to note that the retrieval of ash concentrations and aerosol particle size information is beyond the scope of this study. We have already noted that the use of temporal thresholds and some of the spatial thresholds used in this paper is not routinely done by standard algorithms (i.e. Prata, 1989). After classifying the volcanic ash pixels, we need to determine the accuracy of the algorithm but this is a difficult task to accomplish. We have chosen to intercompare the SEVIRI algorithm results with MODIS and MISR products by making the assumption that their identification is correct. We take this a step further by comparing our results with aircraft data but not many data points can be obtained with such a comparison. This is not a unique problem to our study since all validation methods have to use a verification source and then provide results and analysis.

Table 1 shows the SEVIRI channels with the center, minimum, and maximum wavelengths for each channel. These channels have a sampling distance of 3 km at sub-satellite point (Schmetz et al., 2002). The channels used to develop the SEVIRI algorithm are highlighted while the channels ignored are primarily used for water vapor, ozone, and carbon dioxide detection. Thus, the SEVIRI algorithm uses three channels in the solar spectrum and four channels in the infrared spectrum.

The MODIS onboard the Terra and Aqua polar orbiter satellites have 36 channels over the spectral range from 0.4-14.4 μm with spatial resolutions of 250 m, 500 m, and 1 km (Savtchenko et al., 2004). A Level 2 aerosol optical thickness (AOT) operational product over both ocean and non bright land surfaces is provided by MODIS at a spatial resolution of 10 km (at nadir) by comparing measured reflectances to a lookup table of computed reflectances from a radiative transfer model (Remer, et al., 2005). The reported uncertainties over ocean and non bright surfaces are $\pm 0.03 \pm 0.05\tau$ and $\pm 0.05 \pm 0.15\tau$, respectively, where τ is aerosol optical depth (AOD) or AOT (Remer, et al., 2005). Additionally, the MODIS Deep Blue Algorithm provides AOT values over deserts and other bright surfaces where the reported uncertainties are approximately 20-30% (Hsu et al., 2006). The Multi-angle Imaging SpectroRadiometer (MISR) instrument onboard the Terra satellite measures upwelling shortwave radiance in four spectral channels (446, 558, 672, and 867 nm) with nine view angles and spatial resolutions of about 250 m to 1.1 km. To produce the MISR Level 2 product (MIL2SAE, F12, 22) with a spatial resolution of 17.6 km, top-of-atmosphere radiances from 16 x 16 pixel areas of 1.1 km resolution are analyzed (Diner et al. (1999). The multispectral and multiangle instrument retrieves accurate AOT values, even over bright deserts (Christopher and Wang, 2004, Kahn et al., 2005), with expected uncertainties of ±0.05 for AOT<0.5 and ±10% for AOT>0.5 (Martonchik et al., 1998). We use the aerosol spatial distribution from MODIS and MISR to help verify the SEVIRI results that we have developed in this paper.

A valuable validation data set used in this study is from the FAAM BAe146 research aircraft data that retrieves detailed volcanic ash measurements from the Leosphere 355 nm Lidar, the Passive Cavity Aerosol Spectrometer Probe (PCASP), and the Cloud and Aerosol Spectrometer (CAS) (Marenco et al., 2011). The FAAM BAe146 aircraft flew on six days in May 2010 where aerosol extinction and AOTs at 355 nm were retrieved along with ash mass concentrations and size distributions (Marenco et al., 2011). This study focuses on 16 May and 17 May since the volcanic ash was associated with higher AOTs on these days. We utilized the AOT measurements at 355 nm retrieved from the lidar which samples the atmosphere from 2 km above the surface to 300 m below the aircraft. Thus, the lidar AOTs exclude any boundary layer contribution, except for the 17 May case where boundary layer aerosols contribute less the 0.05 to the AOT. After integrating the AOT measurements over every minute, each retrieved AOT value corresponded to an along-track distance of 8-10 km. Note that AOT can still be derived in the presence of clouds by using the instruments onboard the BAe146 aircraft to detect and mask the cloud contaminated areas in the vertical column of air beneath the aircraft. The usefulness of BAe146 aircraft measurements has been shown in a number of papers where the aircraft measurements were analyzed along with satellite measurements (Johnson et al., 2012, Christopher et al., 2009, Naeger et al., 2013).

3. Methodology

There is a rich heritage of classification algorithms with the most common ones using the concept of spectral signatures where for example clouds 'look different' based on spectral signatures in some wavelengths when compared to aerosols and land. A classic paper by Saunders and Kriebel (1988) used spectral and some spatial signatures to separate pixels into cloud-free, partly cloudy, or overcast scenes. Using spectral thresholds alone can cause uncertainties in image classification since there could be spectral overlap between and among classes. Thus, it is not possible to accurately separate various classes based on limited information from spectral signatures alone

(Ackerman et al., 2008). For example, Fig. 1 is a SEVIRI RGB image on 17 May 2010 at 1330 UTC over Europe and the Atlantic Ocean where we **carefully hand picked 28 samples representing volcanic ash, cloud, and clear sky ocean and land surfaces. We do not show a typical dust RGB (e.g. Francis et al., 2012) in Fig. 1 because regions of cloud can be difficult to visually separate from the underlying surface in the dust RGB. Instead, the RGB image in Fig. 1 was produced by assigning the BTD 12.0-10.8 values as the red component, the 0.6 μm reflectance as the green component, and the BTD 10.8-8.7 as the blue component. By using the 0.6 μm channel we could more easily see where small scale clouds were located over both land and ocean allowing us to pick better samples. Note that we also hand picked 28 samples on two other days during the Eyjafjallajökull volcanic eruption period, 7 May at 1100 UTC and 18 May at 1600 UTC. Overall, we hand picked 18 samples of ash over water, 6 samples of ash over land, 30 samples of cloud, and 30 samples of clear sky ocean and land.** Fig. 2a is a wavelength versus reflectivity plot for the three SEVIRI reflectivity channels showing the mean **along with minimum and maximum reflectance for the 80 extracted samples where the ocean is blue, land is green, ash over water is red, ash over land is pink, ash above cloud is light blue, and cloud is black.** Fig. 2b is the same as Fig. 2a except wavelength versus temperature for four SEVIRI temperature channels is displayed. For the reflectivity channels, the **cloudy samples generally have a much higher reflectivity than the ocean while the mean reflectivity of ash over water is only about 5-10% higher than the ocean. However, note the large variation in the reflectance of the cloud and ash samples that make it difficult to use spectral tests alone to separate these features. Nonetheless, in general, the reflectance is staying rather constant or increasing for the cloudy samples when moving from the 0.6 to 1.6 μm channels while the reflectance is decreasing for the ash over water samples.** The mean ash reflectivity drops to only about 6% at 1.6 μm which is mostly due to the fact that the majority of ash particles are generally smaller than this channel wavelength (Weber et al., 2012). **Thus, spectral tests using the difference of two reflectivity channels can be used to better separate features.** When analyzing the temperature trend between the 10.8 and 12.0 μm channels in Fig. 2b, the temperature generally increases with wavelength for ash but decreases for the other features which is due to the unique characteristic of the ash imaginary refractive index being higher at 12.0 than at 10.8 μm causing the slightly lower temperatures at 12.0 μm (**Prata**, 1998). **However, once again a large variation in the temperatures of the various features exists which makes it difficult to use only spectral tests for developing an accurate classification algorithm.** Martins et al. (2002) showed the utility of using spatial (textural) measures to separate aerosols from clouds over oceans due to the mean and standard deviation for a group of aerosol pixels being different than clouds. Spatial measures are a form of texture identification where a group of aerosol pixels appear different than clouds due to several measures and one example being their homogeneity. Therefore, combining spectral and spatial information reduces the frequency of misclassifications within an image.

In this paper, we take this a step further by using temporal information along with spectral and spatial information as the high temporal resolution of geostationary satellite sensors permits the use of these tests, but only a handful of studies have actually used temporal tests (Calle et al., 2006, de Wildt et al., 2007). Calle et al. (2006) proposed a fire detection technique that utilized temporal information from the 3.9 μm SEVIRI channel and showed that false alarm rates were lower than when detecting fires without using any temporal information. Typically the temperature from the 3.9 μm channel does not encounter large variations with time, but Calle et al. (2006) found that large increases occur with the onset of fires which helps better detection of fires. Cloud detection can also be improved when using temporal information since the temporal variation of the reflectance and temperature of a pixel is usually greatly impacted by the presence of clouds. For example, when analyzing the reflectance of the 0.6 μm SEVIRI channel for a pixel over a period of time, the variation in the reflectance will be minimal in most clear sky cases but rather large for most cases where clouds are present since clouds are typically much more heterogeneous than the underlying land surface. Then, de Wildt et al. (2007) developed temporal tests using reflectance and temperature channels from SEVIRI and found that these tests helped mask clouds and cloud shadows which ultimately led to more accurate detection of snow cover. Although the temporal tests detected most clouds due to their heterogeneity, they had to rely on the spectral tests to detect the water clouds that were rather homogeneous since the reflectance and temperature channels showed little temporal variation. Another issue that often arises when using temporal techniques is the overestimation of cloud cover especially in areas near cloud edges and in areas over broken clouds where a pixel may be cloud free in the current time-step but cloudy in the previous one. This situation can cause a significant increase in the variation of reflectance and temperature with time for a cloud free pixel. **Furthermore, freshly emitted volcanic ash may be detected as cloud when using temporal techniques since the reflectance and temperature of the pixel can vary significantly with time.** Therefore, even though temporal techniques have been used successfully for detecting fires and clouds, they also encounter problems that are investigated further in this study. **For instance, freshly emitted volcanic ash plumes can cause large temporal variations**

3.1 General flow of algorithm

For our algorithm, we first identify pixels that are land (or over land) and pixels that are water (or over water) to make the algorithm efficient and save computational time. This is necessary since the thresholds used to identify aerosols and clouds are different over water than over land. Classification methods are usually easier over water since water has a low visible reflectance and warmer infrared temperatures when compared to aerosols and clouds. However, over land spectral tests pose challenges since the surface reflectance and temperatures can be highly variable. After separating land and water pixels, we identify feature pixels through a temporal test over all surfaces along with a spectral test over only water. Feature pixels are simply pixels that are contaminated with any type of aerosol or cloud. Then, all pixels labeled as feature are fed into the second part of the algorithm that identifies cloudy pixels through spectral, spatial, and temporal tests. If the feature pixel passes any one of these tests, then it is labeled as cloud. If the pixel fails all of these tests, then the pixel is labeled as aerosol. Since the aerosol spatial distribution maps can be produced every **5** minutes when using SEVIRI, they can provide near real-time information on the location of volcanic ash which is a major aviation concern (Casadevall, 1992). Also, understanding the spatial distribution of aerosol and cloud is very important as this is the first step to accurately quantifying the cloud and aerosol radiative forcing (Kaufman et al., 2002).

3.2 Input data for algorithm

The U.S. Geological Survey (USGS) global land cover characteristics database version 2.0, SEVIRI viewing and solar zenith angles, and the SEVIRI channels highlighted in Table 1 are input into our algorithm. SEVIRI viewing and solar zenith angles are primarily used for masking sun glint regions while the SEVIRI channels provide the critical reflectivity and temperature values for each pixel. The USGS global land cover data is used immediately in the algorithm to separate land and water pixels and to find bright (e.g. desert) and non-bright (e.g. vegetation) pixels over land since certain threshold tests are not valid over bright surfaces with high reflectivity. Next, we develop a clear sky reflectance map by finding the minimum top of atmosphere (TOA) 0.6 μm reflectance for each pixel **over a 14 day period (**Jolivet, et al., 2008). **In order for this algorithm to be used operationally, the 14 days prior to the time of interest is used to find the minimum TOA reflectance for a pixel**. For example, if analyzing a 1300 UTC SEVIRI image on 19 April 2010, then we find the minimum 0.6 μm reflectance from **5 April until 19 April** at 1300 UTC for each pixel which generates the clear sky reflectance map. For bright surfaces determined by the USGS global land cover map, we find the highest 10.8 μm temperature during the 14 day period and then extract the 0.6 μm reflectance from this particular pixel. Dust over desert regions can reduce the observed TOA reflectance below the actual clear-sky reflectance since dust is slightly absorbing at 0.6 μm (Patadia et al., 2009).

3.3 Algorithm Over Land

After generating the clear sky reflectance maps, the algorithm over land begins with a snow detection scheme (not shown in Table 2) so that these bright pixels can be ignored throughout the remainder of the algorithm. This snow detection scheme uses the normalized difference snow index (NDSI), which takes advantage of snow being more reflective at 0.6 μm than at 1.6 μm (Riggs and Hall, 2004), along with other temporal tests. For all the temporal tests used in Table 2, the standard deviation (σ) of three successive 15 minute SEVIRI images centered on the current image is computed for the highlighted channels in Table 1. Temporal tests help reduce the frequency of falsely detected clouds as snow (Riggs and Hall, 2004), and for this study we use the σ of the 1.6 and 10.8 μm as the reflectance and temperature of snow generally varies slowly with time (de Wildt et al., 2007). However, we will not go any further into the specifics of the snow detection scheme because it is not critical to the main goal of the algorithm and the results of this paper.

The first test in Table 2, which uses the 0.6 μm clear sky reflectance maps to determine whether a pixel is a feature, **is the most important to the success of the algorithm.** If the difference between the 0.6 μm reflectance for the current SEVIRI pixel and its clear sky reflectance is greater than **1.5% (i.e. |0.6 μm$_{cur}$-0.6 μm$_{clr}$| > 1.5%** in Table 2), then the pixel is classified as a feature. The 0.6 μm$_{cur}$-0.6 μm$_{clr}$ test detects features well since in the presence of an atmospheric feature such as ash where the 0.6 μm reflectance is typically higher than in clear sky conditions. Fig. 3 shows bispectral plots for the SEVIRI channels of most interest to this study from the samples **used to produce Fig. 2. The colors represent the same features as in Fig. 2.** Fig. 3a shows the **0.6 μm$_{cur}$-0.6 μm$_{clr}$ values on the x-axis and the BTD10.8-12.0 values on the y-axis. The ocean (blue) and land (green) samples have 0.6 μm$_{cur}$-0.6 μm$_{clr}$ values mostly less than 1.5%. There are a few land pixels with values slightly higher than 1.5% which is likely due to some cloud contamination occurring within the land samples as the persistent cloud cover over land made it difficult to hand pick completely clear sky samples. Nonetheless, there is quite good separation between the clear sky samples and the atmospheric feature samples when analyzing the 0.6 μm$_{cur}$-0.6 μm$_{clr}$ values alone which gives us confidence in using this test. However, there is some significant overlap between the ash (red and pink) and cloud (black) samples which is why this test is only used to separate clear sky and atmospheric feature pixels. Note that we introduce the absolute value in this first test in order to account for scenarios over bright land surfaces where the** higher 0.6 μm clear sky reflectance over these surfaces can completely mask the cloud or aerosol signal. In fact, the presence of an absorbing ash or dust layer over a bright surface can actually reduce the 0.6 μm reflectance below the clear sky reflectance.

The second test in Table 2 which uses the BTD between the 8.7 and 10.8 μm channels (BTD 8.7-10.8) along with BTD 10.8-12.0 has been shown to detect ice clouds quite accurately (Zhang et al., 2006). **Thus, this test is specifically used to detect clouds in our study over all pixels including the feature pixels just detected by the first test. Fig. 3b shows the BTD 8.7-10.8 on the x-axis and BTD 10.8-12.0 on the y-**

axis where there is not as good separation between the various sample types as in Fig. 3a. However, these tests have some utility in separating atmospheric features as the samples with BTD 8.7-10.8 > -2 K and BTD10.8-12.0 > 0 K are nearly all cloud pixels. As a result, we use these threshold values in this test to detect clouds. Also, note that the ash samples (red) that are associated with BTD 8.7-10.8 > -2 K have BTD 10.8-12.0 values primarily less than 0 K which means most ash pixels will not be classified as cloud by this test.

Next, the algorithm separates the feature pixels as cloud or aerosol by using a series of cloud detection tests. If a feature pixel is not labeled as cloud by the cloud detection tests, then the pixel is labeled as aerosol. The first cloud detection test labels pixels as cloud when the 10.8 µm < 240 K and BTD 10.8-12.0 > -0.5 K. Freshly emitted volcanic ash can have a temperature that is closely related to its height so it is possible that the 10.8 µm temperature can be less than 240 K for ash. Therefore, we also include the BTD 10.8-12.0 µm test since freshly emitted volcanic ash will typically have strongly negative values. Fig. 3b shows an example of the strongly negative BTD 10.8-12.0 values that can occur with freshly emitted ash where the fresh ash samples have a BTD 10.8-12.0 µm around -1 K and BTD 8.7-10.8 near 0 K. Then, we apply a test that labels a pixel as cloud if the 1.6 µm > 30% and BTD 10.8-12.0 > -0.5 K. This study found that even the thickest ash regions will typically have 1.6 µm < 30% after picking samples of the freshly emitted ash nearby the Eyjafjallajökull volcano on 7 May. is a scatter plot with the 1.6 µm on the x-axis and BTD 10.8-12.0 on the y-axis which clearly shows that all our samples with 1.6 µm > 30% are cloud contaminated. The next cloud test simply labels the pixel as cloud if the BTD 10.8-12.0 > 1.5 K. Fig. 3c shows the utility of this test as ash samples all have BTD 10.8-12.0 < 1.5 K while the cloudy samples are dominant above this threshold. Thin ash (AOD < 0.2) can have very similar BTD 10.8-12.0 as the land surface since areas of thin ash will have minimal impact on terrestrial radiation. Consequently, thin ash regions can potentially be labeled as cloud by this test but only if the $|0.6\ \mu m_{cur}-0.6\ \mu m_{clr}|$ test labels it as a feature. These thin ash regions do not pose a threat to aviation so it is not a major issue if thin ash is missed by our algorithm.

The remaining cloud detection tests in Table 2 utilize either spatial or temporal techniques. In this study, the temporal tests take three successive 15 minute SEVIRI scans and calculate the σ for each pixel which is referred to as a σT test throughout the remainder of the paper. We decided to use only 3 successive SEVIRI images to calculate σ because using more successive images increases the likelihood that both aerosol and cloud could be included in the σ computation for a pixel where aerosol and cloud reside nearby, and we want to limit these scenarios as much as possible. Also, by using only 3 successive images, this algorithm can be used in time sensitive situations, such as volcanic ash plumes interfering with air traffic, that require real-time decision making. We use σT tests with the 1.6 µm channel where the appropriate thresholds were chosen based on analyzing the scatter plot in. All the ash over land samples (pink) were associated with σT 1.6 µm < 1.5% while cloudy samples were dominant above this threshold. Ash plumes are generally more homogeneous than clouds which is the reason for the fairly good separation between ash and cloud samples in Fig. 3d. However, a portion of the cloud samples have very low σT 1.6 µm and cannot be labeled as cloud by this test. The next test in Table 2 uses the |0.6 μm_{cur}-0.6 μm_{clr}| technique along with BTD 10.8-12.0 since we observed good separation between the ash and cloud samples in this multi-spectral space as revealed by Fig. 3a. This test labels clouds when the |0.6 μm_{cur}-0.6 μm_{clr}| > 3.5% and BTD 10.8-12.0 > 0 K. We include the BTD 10.8-12.0 technique in this test since moderate (AOD > 0.5) and thick (AOD > 1.0) ash regions with BTD 10.8-12.0 < 0 K can have |0.6 μm_{cur}-0.6 μm_{clr}| > 3.5%. Thus, by including the BTD 10.8-12.0 technique the moderate and thick ash plumes will generally not be labeled as cloud. In fact, Fig. 3a shows that as the |0.6 μm_{cur}-0.6 μm_{clr}| increases beyond 3.5% the BTD 10.8-12.0 primarily decreases with increasing |0.6 μm_{cur}-0.6 μm_{clr}|. Fig. 3a suggests that this test can be quite powerful in accurately labeling atmospheric features (e.g. cloud and dust) correctly.

The final two tests utilize spatial techniques along with the BTD 10.8-12.0 technique once again. The spatial techniques (i.e. σs tests) compute the σ over a 3 X 3 pixel region. For the first test, if σs 12.0 µm > 1.5 K and the BTD 10.8-12.0 > 0 K, then the center pixel of the 3 X 3 pixel group is classified as a cloud. The σs and σT tests work on the similar principles of cloud typically being more heterogeneous than aerosol except that the σs test operates in space instead of time. **This is demonstrated in Fig. 3e where the cloudy samples tend to have higher σs 12.0 μm values than shown for the ash pixels, but there is considerable overlap between a portion of the cloudy samples and the ash samples. Consequently, we introduce one more spatial test that has the ability to detect many of these cloudy samples that went undetected by the σs 12.0 μm test. This second spatial test labels cloud when the σs 1.2 μm > 1.2% and BTD 10.8-12.0 > 0 K, and the scatter plot that shows the separation of the various samples in this multi-spectral space is displayed in Fig. 3f. We see that the cloudy samples that were associated with very low σs 12.0 μm and BTD 10.8-12.0 near 0 K in Fig. 3e are detectable when using the σs 1.6 μm technique. There is more scatter with the ash samples in Fig. 3f but these ash samples with σs 1.6 μm > 1.2% have mostly BTD 10.8-12.0 < 0 K which means that they will not be labeled as cloud by this test. These are likely thick ash plumes (AOD > 1.0) that tend to be more heterogeneous. However, we do notice that a few ash samples will be incorrectly labeled as cloud since they have BTD 10.8-12.0 > 0 K and σs 1.6 μm > 1.2%. These ash samples were actually taken near the boundaries of thick ash plumes which means this spatial test can encounter problems due to strong boundaries occurring in SEVIRI imagery. Lastly, the feature pixels that fail all of the final cloud detection tests are labeled as aerosol. Note that we do show ash above cloud samples (light blue) in the panels in Fig. 3, but we do not discuss them in the preceding paragraphs. The main point for showing the ash above cloud samples is to stress that it is extremely difficult to separate the ash above cloud from the ash-free cloud samples. The other possible way to separate the ash above cloud from the ash-free cloud samples is by using the BTD 10.8-12.0 technique which our algorithm is using in nearly all the tests. Therefore, this algorithm is capable of detecting ash above cloud samples only if the ash influences a negative BTD 10.8-12.0 value. We will show examples of our algorithm detecting ash above cloud in Section 4.**

3.4 Over Water Algorithm

We briefly discuss the over water algorithm **since it has many similarities to the over land algorithm**. The only differences between the land and water algorithms are the slightly lower thresholds that are used to detect clouds for the **σs 1.6 µm and σs 12 µm techniques and the inclusion of the 1.6 µm – 0.6 µm technique. The threshold is lowered to 1% for the σs 1.6 µm test and 1.0 K for the σs 12 µm test due to the** relative homogeneity of the water. **The 1.6 µm – 0.6 µm test can be quite powerful over the homogeneous water surface as indicated in Fig. 3g where 1.6 µm – 0.6 µm is on the x-axis and the BTD 10.8-12.0 on the y-axis. The clear-sky ocean samples (blue) and ash over water samples (red) have very similar 1.6 µm – 0.6 µm values ranging mostly from -7% to -3%. Even the thick ash samples with BTD 10.8-12.0 near -2.0 K have 1.6 µm – 0.6 µm values no larger than -3%. Nevertheless, we include the BTD 10.8-12.0 technique in this test to ensure that thick ash does not get labeled as cloud. The pixel is labeled as cloud by this test when the 1.6 µm – 0.6 µm > -2% and BTD 10.8-12.0 > -1 K. Similar to the over land algorithm**, after applying all the cloud detection tests to the feature pixels, the pixels that fail all the tests and remain as features are labeled as aerosol.

4. Results and Discussion

4.1 13 May 2010 Case

Fig. 4a is a SEVIRI dust RGB image on 13 April 2010 at 1200 UTC when a substantial amount of ash was being emitted from the Eyjafjallajökull volcano. The dust RGB image was produced by assigning the BTD 12.0-10.8 values as the red component, the BTD 10.8-8.7 as the green component, and the BTD 10.8 µm as the blue component. The volcanic ash is identified in the SEVIRI dust RGB image by the reddish colors extending eastward from Iceland. Fig. 4b is a SEVIRI 0.6 µm visible image where the clouds appear white against a dark background. The visible image shows extensive cloud coverage across the domain with clouds evident in the location of the volcanic ash plume. This ash plume is primarily associated with BTD 10.8-12.0 < 0 K with strongly negative values of -4 K within the core of the plume (i.e. Fig. 4c). Note that a substantial amount of pixels not associated with the main ash plume also possess negative BTD 10.8-12.0 as revealed by the reddish colors in Fig. 4c. According to the SEVIRI dust RGB and the visible image, these pixels are primarily cloudy pixels that do not appear to be associated with any ash. For

instance, the clouds to the southwest of Iceland have a BTD 10.8-12.0 as low as -0.4 K. The final results of the SEVIRI algorithm are in Fig. 4d with the pixels labeled as clear sky (white), cloud (gray), and aerosol (orange). Our algorithm is able to identify the ash plume even though clouds reside beneath it since many of the cloud tests in Table 2 include the BTD 10.8-12.0 technique. Also, the ash free cloudy pixels that were associated with the negative BTD 10.8-12.0 in Fig. 4c are labeled as cloud by our algorithm. Therefore, overall the algorithm performs well for this particular case.

A few pixels are labeled as aerosol outside of the main ash plume which we further investigate by analyzing the MISR and MODIS Aqua AOD around the time of interest (~1300 UTC) on 13 May. Note that MISR has limited spatial coverage due to its limited field of view, but the MISR transect occurring near the center of the domain passes over the eastern section of the ash plume (Fig. 4e). The MISR fails to retrieve any significant area of AOD for the ash plume due to the fact that the retrieval algorithm recognizes the plume as mostly cloud. The MODIS also has difficulty retrieving any AOD for the ash plume due to the extensive cloud coverage in this region. The lack of MISR and MODIS AOD retrievals of the ash plume is not surprising since their algorithms attempt to retrieve AOD for cloud-free regions only. However, the MODIS retrieves AOD where our SEVIRI algorithm labels clear sky pixels across much of the domain. Much of the MODIS AOD across the domain is less than about 0.15 which suggests that the aerosol concentrations are very low. Volcanic ash with low concentrations (< 0.2 g m^{-2}) pose no threat to aviation. Therefore, the fact that our algorithm is not detecting these areas of low AOD is not problematic. Some limited areas of AOD > 0.2 appear just south of Great Britain and southeast of Iceland in the MODIS AOD image which our algorithm mostly identifies as cloud or clear sky. The fact that some of these areas of AOD > 0.2 reside among clouds as seen in the SEVIRI dust RGB and visible image suggest that these may be bad retrievals. For instance, the AOD > 0.2 to the southeast of Iceland is retrieved in a dominantly cloudy region. The retrievals of AOD > 0.2 just south of Great Britian are also occurring either among cloud or adjacent to clouds. It is known that the MODIS AOD tends to have a high bias

when the retrievals are adjacent to clouds (Zhang et al., 2006). Nonetheless, a close inspection of the SEVIRI dust RGB reveals pinkish colors over the ocean just to the south of Great Britain which implies that some ash may be present here. The fact that our algorithm labels some pixels as aerosol in this same location suggests that the MODIS AOD > 0.2 in this particular region may be real. Fig. 4d also reveals that our algorithm may falsely detect aerosols along cloud edges. These false detections are difficult to see in Fig. 4d but there are a few occurrences among the cloud edges to the south of Iceland.

4.2 16 and 17 May 2010 Case

Figs. 5a-f are similar to Figs. 4a-f except that the former pertain to the 17 May 2010 case study at 1300 UTC where a significant area of volcanic ash resided over the North Sea around 56°N and 7°W (Turnbull et al., 2012). **This ash plume is not as apparent on the SEVIRI dust RGB due to the fallout of ash particles during its transport from Iceland. In fact, it is difficult to decipher the ash plume from the low level clouds (yellowish colors) across the domain. Analyzing both the dust RGB and visible image along with the BTD 10.8-12.0 map (i.e. Fig. 5c) helps better understand where the potential ash regions are located. The pink to yellow colors associated with the ash plume in the dust RGB appear darker than the whiter clouds in the visible image across the North Sea. By this time, the ash plume has become only slightly more reflective than the background ocean. There are some clouds among the ash plume that are only noticeable when closely inspecting the visible image which shows the utility of analyzing both the dust RGB and visible image. The BTD 10.8-12.0 map shows a considerable area over the North Sea and Norwegian Sea that has BTD 10.8-12.0 < -1 K suggesting that ash is present across the area. Our algorithm is easily able to identify these areas where the BTD 10.8-12.0 < -1 K and thick ash is likely present.** According to the dust RGB and visible image, our algorithm successfully disregards cloud contaminated areas within the ash plume region over the North Sea. For example, clouds are shown off the coast of the Netherlands (~56°N, 5°E) and this area is labeled as cloud by our algorithm. **Overall, our algorithm appears to identify clouds very well across the domain which is critical as the final aerosol spatial distribution maps depend on the success of the cloud detection. Moreover,**

our algorithm identifies aerosol in locations across the North Sea that have BTD 10.8-12.0 > 0 K and appear to be cloud-free. These results are in fairly good agreement to the spatial distribution of MODIS AOD across the North Sea which implies that our algorithm is performing accurately on this day. MODIS retrieves AOD primarily ranging from 0.2 to 0.4 across the North Sea with the exception of a few higher AOD regions where values near 0.7 are present. The location of the higher AOD regions coincide with BTD 10.8-12.0 < -1 K while the AOD from 0.2 to 0.4 coincide with near zero to positive BTD 10.8-12.0 values. The MISR AOD agrees fairly well with MODIS in the limited locations of MISR availability over the North Sea and Norwegian Sea which gives us better confidence that the MODIS retrievals are good on this day. Although our algorithm is able to detect these areas of optically thinner ash identified by MODIS and MISR, it is likely that they are below the mass concentration threshold of 0.2 g m^{-2} and do not pose a threat to aviation (Francis et al., 2012; Prata and Prata, 2012). Again, our algorithm mostly misses the very low AOD regions below about 0.2 that are detected by MODIS and MISR. For example, our algorithm labels the area just north of Great Britain as clear sky while the MISR and MODIS retrieves AOD around 0.15. Finally, note that our algorithm is able to detect the thick ash over the Norwegian Sea (~64°N, 0°E) even though it is above a considerable area of clouds according to the SEVIRI visible image. Once again, this shows the ability of our algorithm to detect thick ash above cloud which can pose a threat to aviation.

The FAAM BAe146 aircraft flights on 16 and 17 May are very helpful for verifying the proposed SEVIRI algorithm. Fig. 6c is a SEVIRI RGB image on 16 May at 1500 UTC with the intricate BAe146 aircraft flight track shown in white. The BAe146 aircraft took off in southeast England (52.1°N, 0.3°W) at approximately 1255 UTC and landed in northwestern France (47.7°N, 2.1°W) at about 1810 UTC. Fig. 6a has 355 nm AOD from the BAe146 aircraft in red with the corresponding AOD scale on the right y-axis and SEVIRI BTD10.8-12.0 in black with its scale on the left y-axis. The dots along the black line indicate the results from the SEVIRI algorithm along the aircraft flight with green, blue, and red denoting clear, cloud, and aerosol, respectively. Fig. 6b shows SEVIRI BTD10.8-12.0 again in black along with 0.6 μm reflectivity in blue with its scale on the y-axis from 0 to 50%. A nearest pixel approach is used to collocate SEVIRI to the BAe146 aircraft in space while we find the closest SEVIRI overpass time to each point along the BAe146 aircraft track to collocate in time. Thus, 15 minute SEVIRI scans beginning 1130 UTC and ending 1700 UTC were used to produce Fig. 6a-b even though only the 1500 UTC SEVIRI RGB imagery is in Fig. 6c.

The aircraft flight began in cloudy conditions across southeastern England and then headed northwest into an ash plume with scattered clouds as shown by Fig. 6c where the ash is highlighted by the pinkish colors and clouds by the green and yellowish colors. Since clouds were the dominant feature in southern England, AOD was not reported but as the aircraft tracked northwestward the AOD jumped to about 0.2 until thick ash was measured at about 55°N and 4.3°W with an AOD of nearly 0.9. The SEVIRI algorithm accurately classifies clouds in southern England, but then classifies a mix of clear skies, clouds, and aerosols where the low AOD of 0.2 is measured which again suggests that the SEVIRI algorithm has uncertainties in detecting optically thin aerosol regions. However, Fig. 6b shows several significant increases in 0.6 μm reflectivity in the low AOD region which hints at cloud contamination. Furthermore, the aerosol extinction coefficient profiles from the BAe146 aircraft on 16 May shown in Marenco et al. (2011) reveal some low level clouds in the low AOD region which suggests the SEVIRI algorithm is classifying clouds properly in this region. When the AOD reaches nearly 0.9, the SEVIRI algorithm classifies nearly all aerosol pixels adequately except for a few pixels which are associated with 0.6 μm > 40% indicating possible cloud contamination. The aerosol extinction coefficient profiles in Marenco et al. (2011) also indicate low level cloud contamination below the thick ash. Thus, according to the BAe146 aircraft data, the SEVIRI algorithm is accurate in labeling a few cloud pixels among the ash. Then, another region of low AOD is measured by the aircraft before flying over thicker ash around 55.2°N and 3.9°W with an AOD of about 0.7. The aerosol is almost entirely missed by the SEVIRI algorithm in this low AOD region as the algorithm classifies mostly clouds. The highly varying 0.6 μm reflectivity among the low AOD suggests that clouds are a dominant feature in this region. In Marenco et al. (2011), low level clouds are revealed all along this section of the BAe146 flight track further hinting at the accuracy of the SEVIRI algorithm. The algorithm classifies some aerosol pixels in the higher AOD region, but clouds are classified more frequently here as the 0.6 μm reflectivity has a significant increase near the minimum in BTD10.8-12.0 indicating the presence of clouds among the thick ash. Also, fairly thick lower level clouds are shown along the aerosol extinction profiles in Marenco et al. (2011) with this thicker ash region. Next, the aircraft encounters very thin ash along its track as AOD drops to near zero values. As expected the SEVIRI algorithm fails to detect any of this ash and classifies mostly clear skies along this portion of the aircraft track. The aircraft flies over one more noteworthy ash region as AOD jumps to about 0.4 and then quickly drops to 0.2 at about 53.8°N and 2.2°W. The ash associated with the AOD of 0.4 is successfully detected by the algorithm which appears to be cloud-free from analyzing the 0.6 μm reflectivity and aerosol extinction profiles in Marenco et al. (2011). However, immediately as the AOD decreases clouds become an issue once again as the 0.6 μm reflectivity jumps to about 35%.

The 17 May BAe146 aircraft flight is overlaid in white on the SEVIRI RGB image from 1400 UTC on that same day in Fig. 7c. However, for this flight, the aircraft started in northwestern France at 1126 UTC and landed in southeast England at 1658 UTC. As seen in the RGB image, the aircraft encountered the main ash plume over the North Sea while scattered clouds impacted the flight over England and Scotland. Fig. 7a-b are the same as Fig. 6a-b except the aircraft AOD and SEVIRI measurements from 17 May are shown. The times when the aircraft were above the scattered clouds over land are clearly seen in Fig. 7b by the very significant increases in 0.6 μm reflectivity, and the SEVIRI algorithm successfully classifies these regions as cloud. After the first period of scattered clouds over land, the aircraft flies over ocean (~53°N, 2.5°W) before making a west to east path over land. When the aircraft is over the ocean, the SEVIRI algorithm classifies mostly clear skies with a mix of some cloud and aerosol. At this time, 355 nm AOD from the aircraft is very low with most values being less than 0.1 which suggests the SEVIRI algorithm has difficulty detecting aerosol over water when the AOD is < 0.1. The aircraft measures AOD near 0.2 during its brief west-east transect over land, but the SEVIRI algorithm classifies cloud in this region, and the algorithm appears to be correct according to the strong peak in 0.6 μm reflectivity and the BAe146 aerosol extinction profiles along this section of the aircraft track in Marenco et al. (2011). After traversing land, the aircraft immediately encounters the main ash plume when flying over the North Sea as indicated by the large increase in 355 nm AOD to about 0.6 in Fig. 7a. However, the aircraft then descends beneath the ash plume which is why the AOD drops to zero while the SEVIRI algorithm detects aerosols. When the aircraft ascends, it measures the ash plume again as the AOD increases to nearly 0.4 before descending and measuring zero AOD the remainder of its flight path. From analyzing the SEVIRI 0.6 μm reflectivity along with the SEVIRI RGB image, it appears that cloud contamination is very minimal across the main ash plume region. Thus, the algorithm performs very well over the ash plume region as only one cloud pixel is detected amongst the aerosol pixels.

4.3 Validation experiment

In order to obtain a better understanding of the accuracy of our SEVIRI algorithm, we perform an additional experiment where we choose 28 independent samples for three different days and times (i.e. 7 May at 1100 UTC, 11 May at 1300 UTC, and 18 May at 1600 UTC) during the Eyjafjallajökull volcanic eruption period. An example of the 28 samples chosen for the 7 May at 1100 UTC case is shown in Fig. 8a where boxes 1-4 are clear sky ocean, 5-12 are volcanic ash, and 13-28 are clouds. We had very limited clear sky land pixels available on this day which explains why we did not choose any samples of clear sky land. The 84 samples taken on these three days represent the truth. Then, we run our SEVIRI algorithm for these three cases and compare the results against truth samples. Overall, we picked 30 ash over water samples on these three days which gave a total of 1080 individual ash pixels to compare against our algorithm results as the size of the each sample spanned 6 by 6 boxes. According to the truth samples, the algorithm performed very well as 936 of the 1080 pixels were accurately labeled as ash by our algorithm giving a success rate of 87%. Not surprisingly, our algorithm performed even better with identifying clouds. Overall, the 60 samples of clouds that we picked provided us with 2160 individual cloud pixels as truth. Our algorithm successfully labeled 2127 of these truth pixels as cloud which gives a 98% success rate for cloud identification. Of course, when performing a validation experiment where we are carefully hand picking truth samples, it is easy to make an algorithm appear more accurate than reality by choosing samples that should be easy for the algorithm to

handle. For this validation experiment, we chose samples that, in our opinion, would be easy to very difficult for the algorithm to identify. Finally, we present the SEVIRI algorithm results for the 7 May at 1100 UTC case where the majority of the ash plume is accurately labeled by the algorithm. This is another case where ash resided above clouds which can make it difficult to identify the ash due to the presence of the cloud. In fact, our algorithm is not able to identify the full extent of the ash plume since the BTD 10.8-12.0 values increase to near or above 0 K. As a result, our algorithm recognizes parts of the ash plume as cloud.

5. Conclusions

In this study we have developed a unique algorithm combining spectral, spatial, and temporal threshold tests using SEVIRI measurements to separate between clear skies, clouds, and aerosols. The algorithm is capable of detecting both dust and ash, but for this paper we only focus on the Eyjafjallajokull volcanic eruption period during April and May 2010 where substantial ash was transported from the volcano to over the North Sea and Europe. Aerosol (e.g. ash) spatial distribution maps were generated every hour during the daytime beginning with the initial eruption on 14 April and ending on 23 May. In this paper we focus specifically on the daytime volcanic ash cases on **13 May**, 16 May, and 17 May when numerous sources of validation data were available. By using MODIS, MISR, and BAe146 aircraft data as verification data, we show that the algorithm is capable of generating accurate aerosol spatial distribution maps **for solar zenith angles < 65°.** First, the SEVIRI aerosol spatial distribution maps show important similarities to the MODIS and MISR AOD products which suggests that the proposed algorithm works well. Second, the BAe146 aircraft shows that the SEVIRI algorithm detects nearly all ash regions over both land and water when AOD > 0.2. However, the MODIS, MISR, and BAe146 aircraft data suggests that the algorithm may encounter some problems detecting ash when AOD < 0.1 over water and AOD < 0.2 over land. **We noticed that at solar zenith angles > 65° the aerosol plumes that were once identified by our algorithm begin converting to cloud. Another major limitation of this algorithm is that it can only be applied during daytime, and for these high latitude regions daytime hours can be severely limited.**

Since the damaging effects of volcanic ash to commercial airplanes can be life threatening, accurately tracking ash during volcanic eruption periods is vital. Polar orbiting satellite sensors do not have the temporal resolution to effectively track volcanic ash. Thus, geostationary sensors, such as SEVIRI, are absolutely critical for tracking volcanic ash and ensuring the safety of people onboard commercial airplanes. The accurate aerosol spatial distribution maps which can be generated every 15 minutes by the proposed SEVIRI algorithm can serve as an extremely important tool during volcanic eruptions.

Acknowledgements. This research is sponsored by NASA's Radiation Sciences, and ACMAP programs. Special thanks to Jim Haywood, Ben Johnson, and Franco Marenco for the aircraft data used in this paper.

Figures

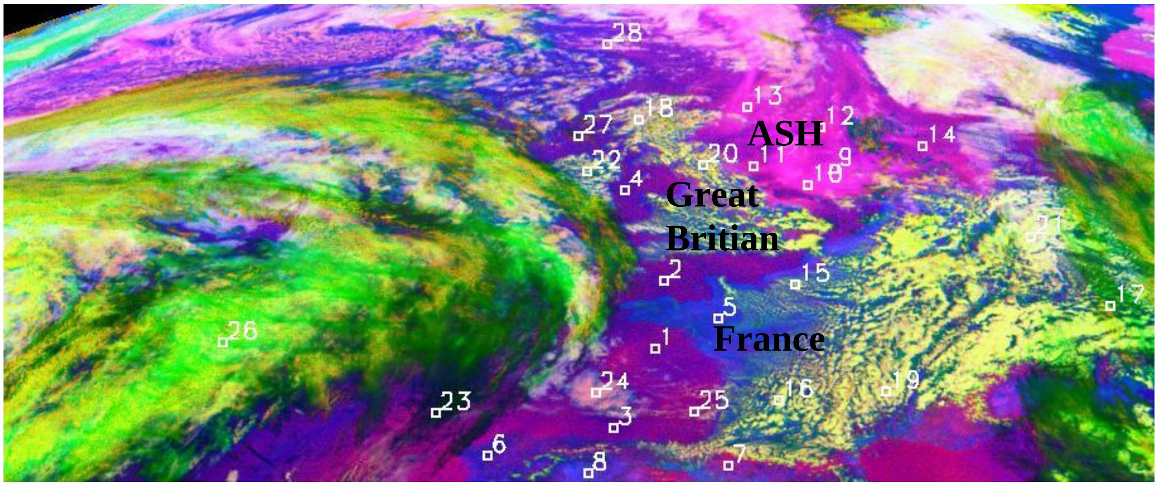

Fig. 1

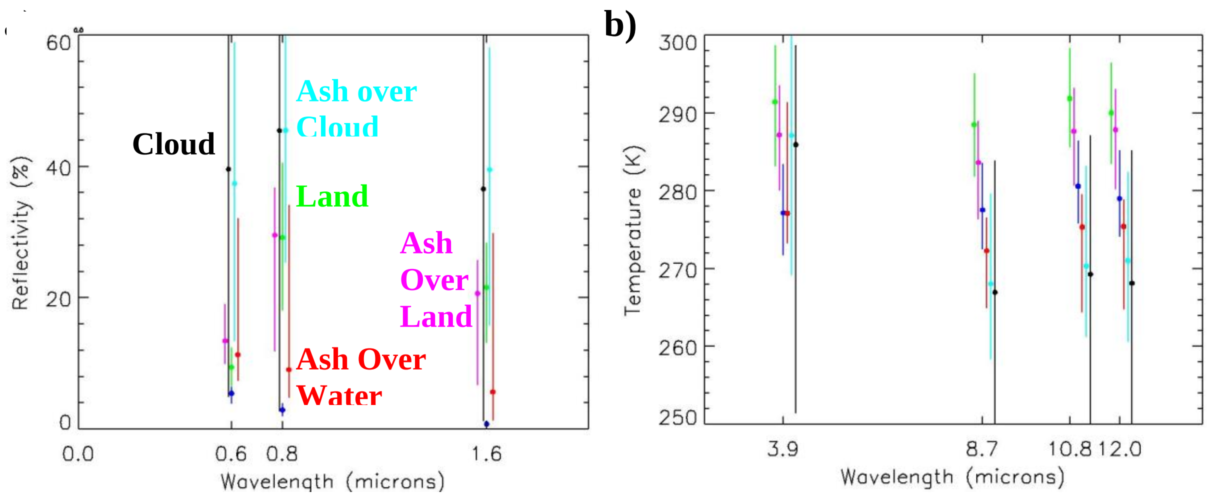
b)
Cloud
Ash over Cloud
Land
Ash Over Land
Ash Over Water
Reflectivity (%)
60
40
20
0
0.0
0.6
0.8
1.6
Wavelength (microns)
Temperature (K)
300
290
280
270
260
250
3.9
8.7
10.8
12.0
Wavelength (microns)

Fig. 2

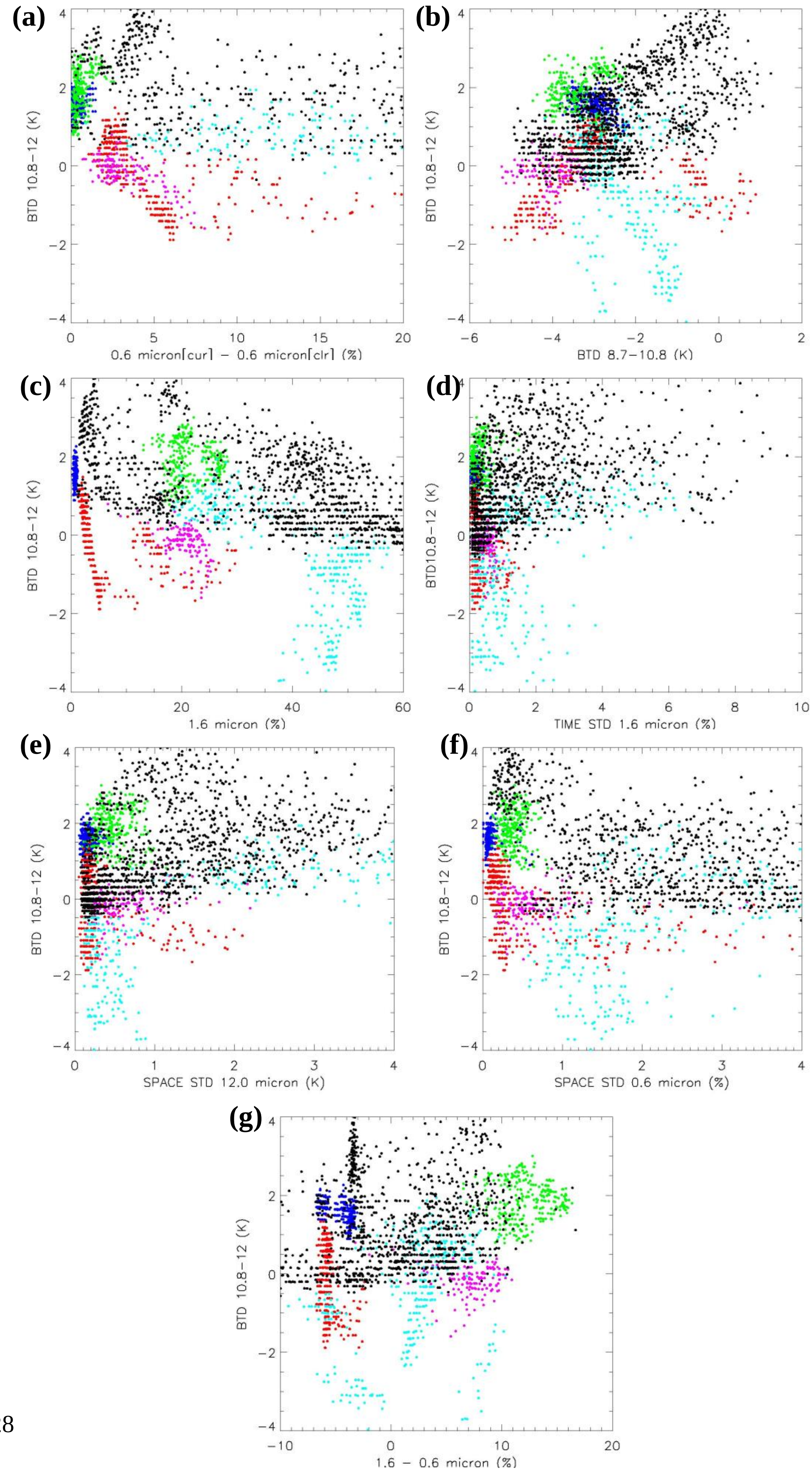
(a)
BTD 10.8−12 (K)
0.6 micron[cur] − 0.6 micron[clr] (%)
(b)
BTD 10.8−12 (K)
BTD 8.7−10.8 (K)
(c)
BTD 10.8−12 (K)
1.6 micron (%)
(d)
BTD10.8−12 (K)
TIME STD 1.6 micron (%)
(e)
BTD 10.8−12 (K)
SPACE STD 12.0 micron (K)
(f)
BTD 10.8−12 (K)
SPACE STD 0.6 micron (%)
(g)
BTD 10.8−12 (K)
1.6 − 0.6 micron (%)

Fig. 3

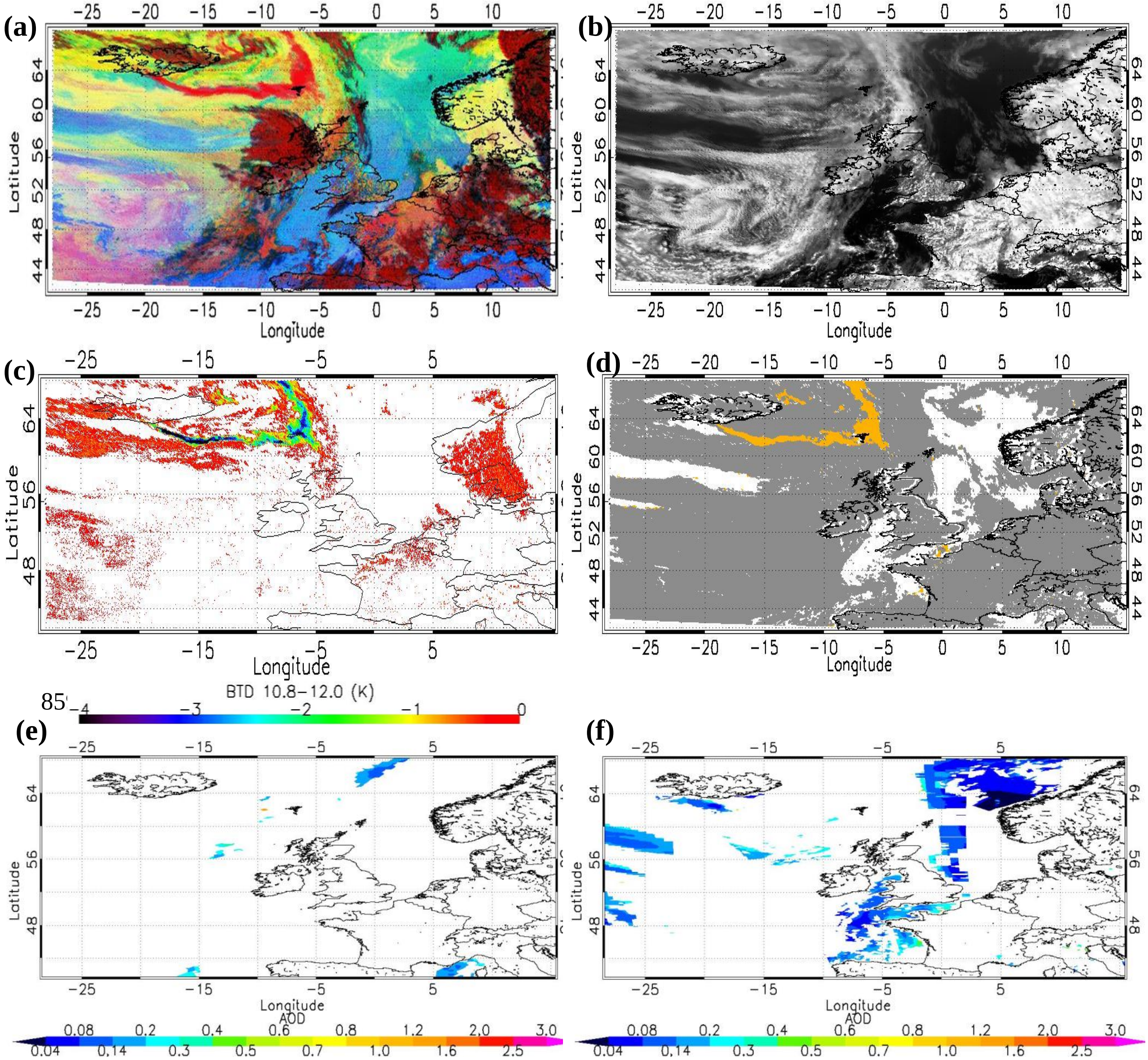
(a)
(b)
(c)
(d)
(e)
(f)
Latitude
Longitude
BTD 10.8−12.0 (K)
AOD
0.04
0.08
0.14
0.2
0.3
0.4
0.5
0.6
0.7
0.8
1.0
1.2
1.6
2.0
2.5
3.0

Fig. 4

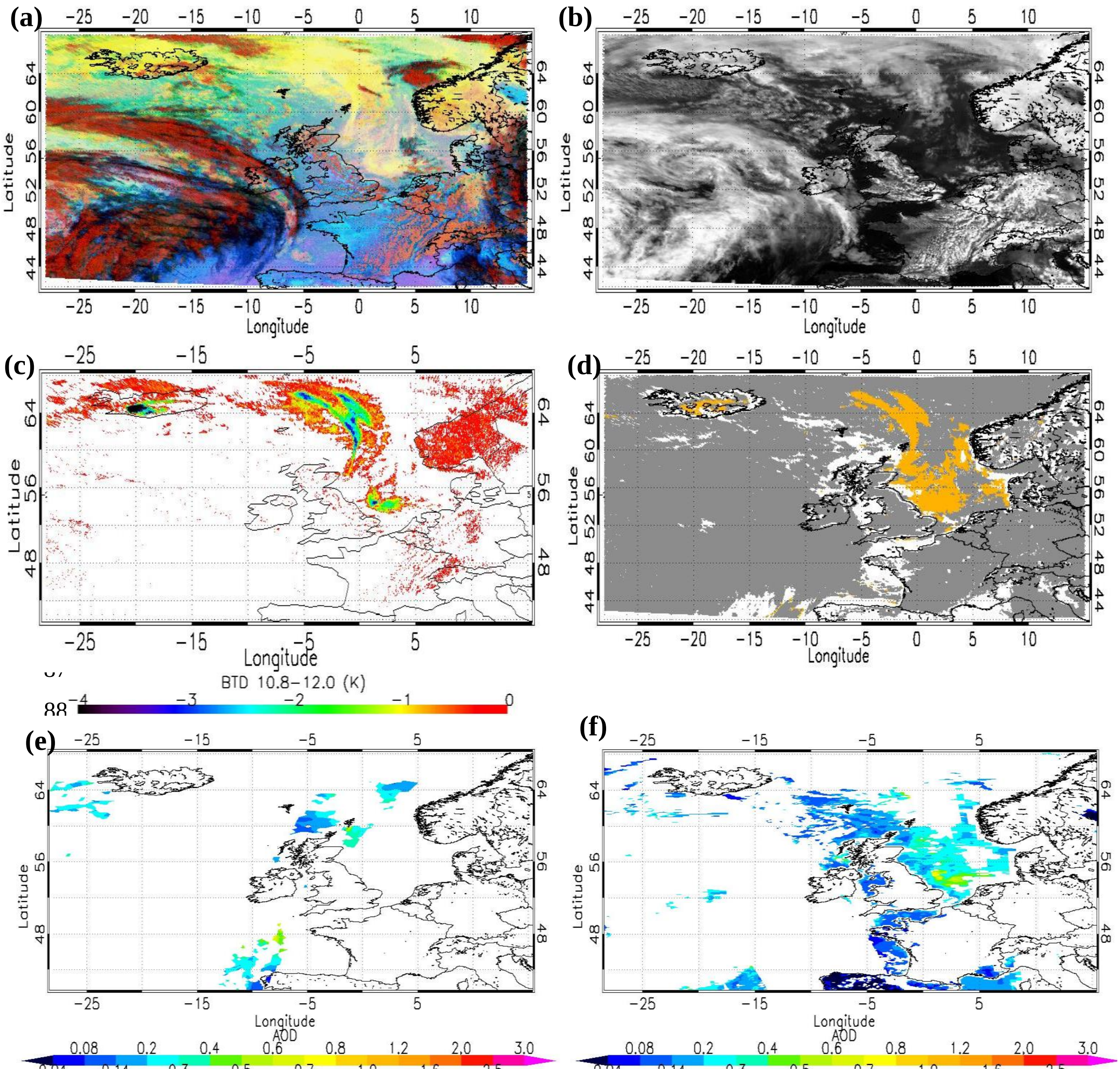
(a)
(b)
(c)
(d)
(e)
(f)
Latitude
Longitude
BTD 10.8−12.0 (K)
−4 −3 −2 −1 0
AOD
0.04 0.08 0.14 0.2 0.3 0.4 0.5 0.6 0.7 0.8 1.0 1.2 1.6 2.0 2.5 3.0

Fig. 5

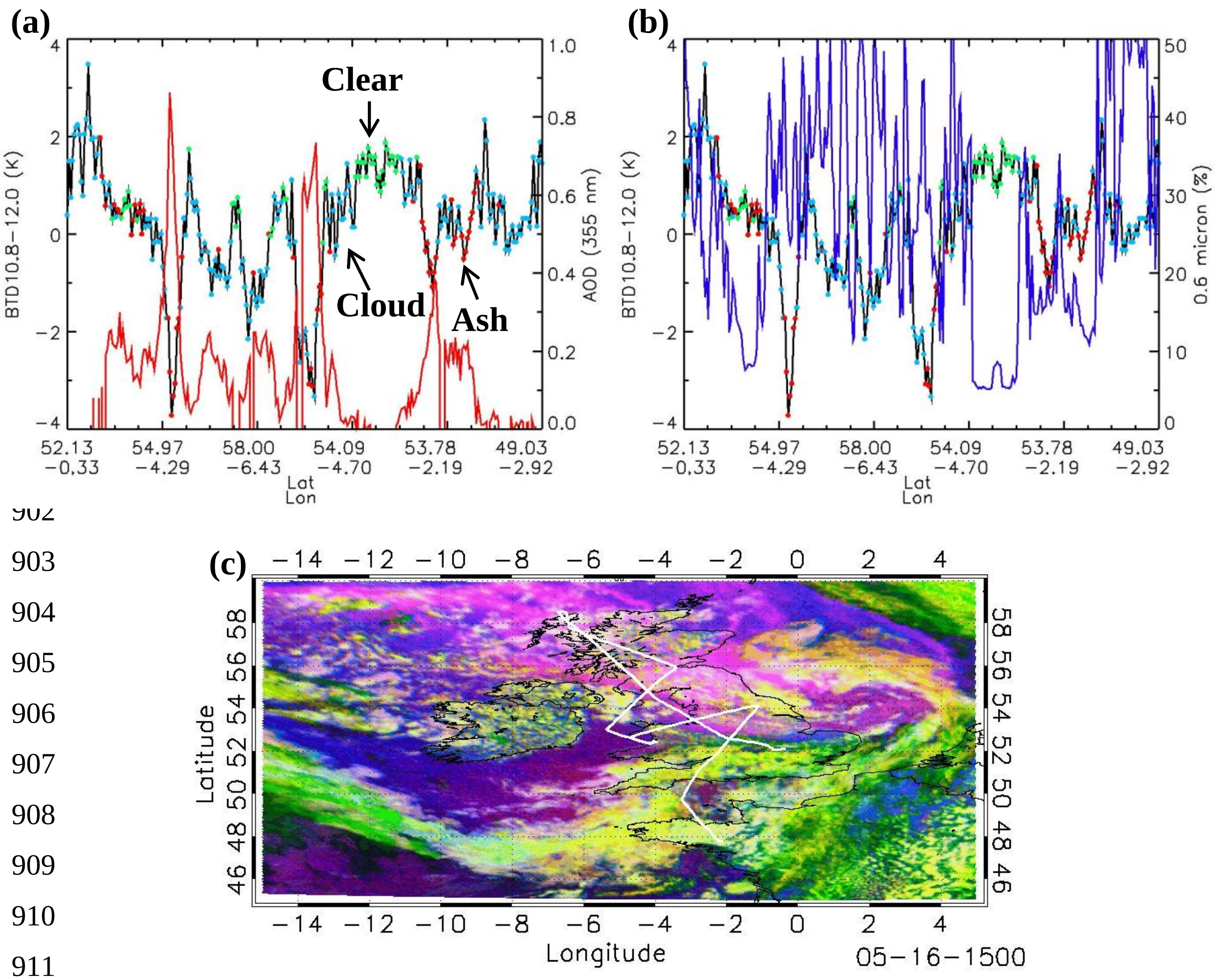
(a)
Clear
Cloud
Ash
BTD10.8−12.0 (K)
AOD (355 nm)
Lat
Lon
52.13 −0.33
54.97 −4.29
58.00 −6.43
54.09 −4.70
53.78 −2.19
49.03 −2.92
(b)
0.6 micron (%)
(c)
Latitude
Longitude
05−16−1500

Fig. 6

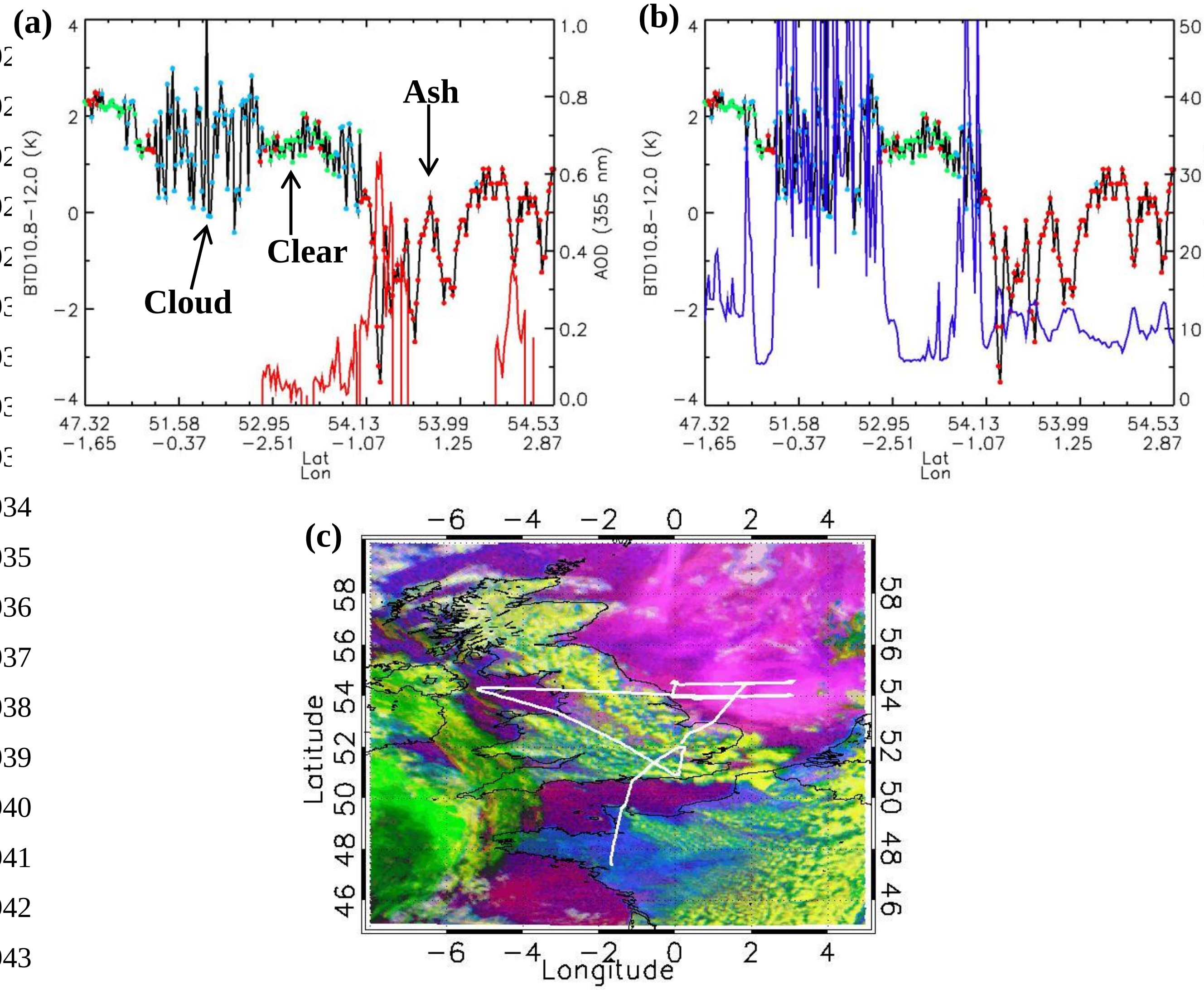
(a)
Ash
Clear
Cloud
BTD10.8−12.0 (K)
AOD (355 nm)
47.32 51.58 52.95 54.13 53.99 54.53
−1.65 −0.37 −2.51 −1.07 1.25 2.87
Lat
Lon
(b)
BTD10.8−12.0 (K)
0.6 micron (%)
47.32 51.58 52.95 54.13 53.99 54.53
−1.65 −0.37 −2.51 −1.07 1.25 2.87
Lat
Lon
(c)
Latitude
Longitude

Fig. 7

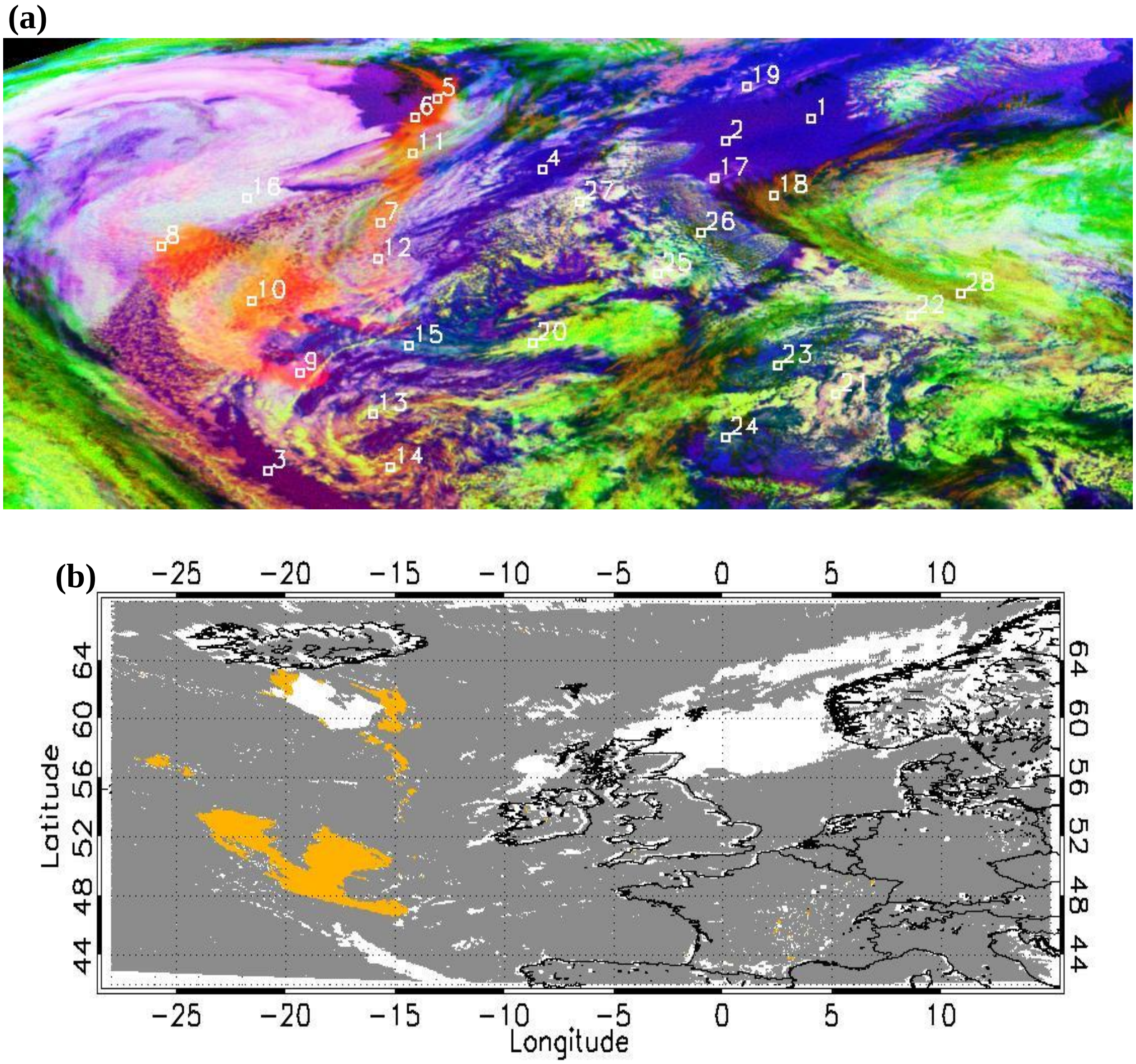
(a)
1
2
3
4
5
6
7
8
9
10
11
12
13
14
15
16
17
18
19
20
21
22
23
24
25
26
27
28
(b)
−25 −20 −15 −10 −5 0 5 10
64 60 56 52 48 44
Latitude
Longitude

Fig. 8

Fig. Legends

Fig. 1. SEVIRI RGB image **(see text for details)** on 17 May 2010 at 1330 UTC over Europe and the Atlantic Ocean **where the 28 boxes indicate the location of extracted samples for various scenes of clear sky water (boxes 1-4), clear sky land (boxes 4-8), ash over water (boxes 9-14), and cloud (boxes 15-28).**

Fig. 2. a) Wavelength versus reflectivity plot for the three SEVIRI reflectivity channels showing the mean **along with minimum and maximum reflectance for the 80 extracted samples where the ocean is blue, land is green, ash over water is red, ash over land is pink, ash above cloud is light blue, and cloud is black.** b) Same as panel (a) except wavelength versus temperature for four SEVIRI temperature channels is displayed.

Fig. 3. Bispectral plots for the SEVIRI channels of most interest to this study from the samples in Fig. 2 where ocean is **blue, land is green, ash over water is red, ash over land is pink, ash above cloud is light blue, and cloud is black.** a) **0.6 μm_{cur}-0.6 μm_{clr} versus** BTD 10.8-12.0, b) BTD 8.7-10.8 versus BTD 10.8-12.0, c) 1.6 μm versus BTD 10.8-12.0, d) **σT 1.6 μm versus BTD 10.8-12.0, e)** σs 12.0 μm versus BTD 10.8-12.0, e) σs 0.6 μm versus BTD 10.8-12.0, and f) 1.6 μm – 0.6 μm versus BTD 10.8-12.0.

Fig. 4. a) SEVIRI dust RGB image on 13 May 2010 at 1200 UTC when a substantial amount of ash was being emitted from the Eyjafjallajökull volcano. The volcanic ash is identified in the SEVIRI RGB image by the reddish colors extending east of Iceland. b) SEVIRI 0.6 µm visible image where clouds appear white against a dark background. c) BTD 10.8-12.0 map. d) Final results of the SEVIRI algorithm with the pixels labeled as clear sky (white), cloud (gray), and aerosol (orange). e) MODIS Aqua AOD results for 13 May where MODIS pixels with cloud fraction larger than 80% are removed. f) MISR AOD across the region on this day.

Fig. 5. Panels (a)-(f) are same as in Fig. 4 except that this is a SEVIRI RGB image on 17 May 2010 at 1300 UTC where a significant area of volcanic ash resided over the North Sea around 56°N and 7°W.

Fig. 6. a) 355 nm AOD from the BAe146 aircraft in red with the corresponding AOD scale on the right y-axis and SEVIRI BTD10.8-12.0 in black with its scale on the left y-axis. The dots along the black line indicate the results from the SEVIRI algorithm along

the aircraft flight with green, blue, and red denoting clear, cloud, and aerosol, respectively. b) SEVIRI BTD10.8-12.0 again in black along with 0.6 μm reflectivity in blue with its scale on the y-axis from 0 to 50%. c) SEVIRI RGB image on 16 May at 1500 UTC with the intricate BAe146 aircraft flight track shown in white. The BAe146 aircraft took off in southeast England (52.1°N, 0.3°W) at approximately 1255 UTC and landed in northwestern France (47.7°N, 2.1°W) at about 1810 UTC.

Fig. 7. Panels a-b) are the same as panels a-b) in Fig. 6 except the aircraft AOD and SEVIRI measurements from 17 May are shown here. c) The 17 May BAe146 aircraft flight is overlaid in white on the SEVIRI RGB image from 1400 UTC where the aircraft took off in northwestern France at 1126 UTC and landed in southeast England at 1658 UTC.

Fig. 8. a) SEVIRI RGB image on 7 May 2010 at 1100 UTC over Europe and the Atlantic Ocean where the 28 boxes indicate the location of extracted samples for various scenes of clear sky water (boxes 1-4), ash above cloud (boxes 5-12), and ash free cloud (boxes 13-28). b) SEVIRI algorithm results for this 7 May case.

References

Ackerman, S. A.: Remote sensing aerosols using satellite infrared observations, J. Geophys. Res., 102, 17069-17079, 10.1029/96jd03066, 1997.

Ackerman, S. A., Strabala, K. I., Menzel, W. P., Frey, R. A., Moeller, C. C., and Gumley, L. E.: Discriminating clear sky from clouds with MODIS, J. Geophys. Res., 103, 32141-32157, 10.1029/1998jd200032, 1998.

Ackerman, S. A., Holz, R. E., Frey, R., Eloranta, E. W., Maddux, B. C., and McGill, M.: Cloud detection with MODIS. Part II: Validation, Journal of Atmospheric and Oceanic Technology, 25, 1073-1086, 2008.

Ansmann, A., Tesche, M., Groß, S., Freudenthaler, V., Seifert, P., Hiebsch, A., Schmidt, J., Wandinger, U., Mattis, I., Müller, D., and Wiegner, M.: The 16 April 2010 major volcanic ash plume over central Europe: EARLINET lidar and AERONET photometer observations at Leipzig and Munich, Germany, Geophysical Research Letters, 37, 2010.

Ansmann, A., Tesche, M., Seifert, P., Groß, S., Freudenthaler, V., Apituley, A., Wilson, K. M., Serikov, I., Linné, H., Heinold, B., Hiebsch, A., Schnell, F., Schmidt, J., Mattis, I., Wandinger, U., and Wiegner, M.: Ash and fine-mode particle mass profiles from EARLINET-AERONET observations over central Europe after the eruptions of the Eyjafjallajökull volcano in 2010, Journal of Geophysical Research D: Atmospheres, 116, 2011.

Brindley, H. E.: Estimating the top-of-atmosphere longwave radiative forcing due to Saharan dust from satellite observations over a west African surface site, Atmospheric Science Letters, 8, 74-79, 2007.

Calle, A., Casanova, J. L., and Romo, A.: Fire detection and monitoring using MSG Spinning Enhanced Visible and Infrared Imager (SEVIRI) data, Journal of Geophysical Research G: Biogeosciences, 111, 2006.

Casadevall, T. J.: Volcanic hazards and aviation safety. Lessons from the past decade, 1992, 210-220.

Christopher, S. A., and Wang, J.: Intercomparison between multi-angle imaging spectroradiometer (MISR) and sunphotometer aerosol optical thickness in dust source regions over China: implications for satellite aerosol retrievals and radiative forcing calculations, Tellus Series B-Chemical and Physical Meteorology, 56, 451-456, 2004.

Christopher, S. A., Johnson, B., Jones, T. A., and Haywood, J.: Vertical and spatial distribution of dust from aircraft and satellite measurements during the GERBILS field campaign, Geophysical Research Letters, 36, L06806, 10.1029/2008gl037033, 2009.

Christopher, S. A., N. Feng, A. R. Naeger, B. T. T. Johnson, and F. Marenco Satellite Remote Sensing Analysis of the 2010 Eyjafjallajokull Volcanic Ash Cloud over the North Sea during May 4 - May 18, 2010, J. Geophys. Res, 10.1029/2011JD016850, 2012.

Diner, D.J., Abdou, W.A., Ackerman, T.P., Crean, K., Gordon, H.R., Kahn, R.A., Martonchik, J.V., McMuldrock S., Paradise, S.R., Pinty, B., Verstraete, M.M., Wang, M., West R.: Level 2 Aerosol Retrieval Algorithm Theoretical Basis, Rep. D11400, Rev. D, Jet Propulsion Laboratory, Pasadena, California, 1999.

de Ruyter de Wildt, M., Seiz, G., and Gruen, A.: Operational snow mapping using multitemporal Meteosat SEVIRI imagery, Remote Sensing of Environment, 109, 29-41, 2007.

Gudmundsson, M. T., et al., SCIENTIFIC REPORTS, 2 : 572, DOI: 10.1038/srep00572 1, 2013.

Hsu, N. C., Si-Chee, T., King, M. D., and Herman, J. R.: Deep Blue Retrievals of Asian Aerosol Properties During ACE-Asia, Geoscience and Remote Sensing, IEEE Transactions on, 44, 3180-3195, 2006.

Johnson, B., Turnbull, K., Brown, P., Burgess, R., Dorsey, J., Baran, A. J., Webster, H., Haywood, J., Cotton, R., Ulanowski, Z., Hesse, E., Woolley, A., and Rosenberg, P.: In situ observations of volcanic ash clouds from the FAAM aircraft during the eruption of Eyjafjallajökull in 2010, Journal of Geophysical Research: Atmospheres, 117, D00U24, 10.1029/2011JD016760, 2012.

Jolivet, D., Ramon, D., Bernard, E., Deschamps, P. -Y., Riedi, J., Nicolas, J. -M., & Hagolle, O.: Aerosol monitoring over land using MSG/SEVIRI. EUMETSAT Meteorological Satellite Conference, Darmstadt, Germany, 8-12 September, 2008.

Kahn, R. A., Gaitley, B. J., Martonchik, J. V., Diner, D. J., Crean, K. A., and Holben, B.: Multiangle Imaging Spectroradiometer (MISR) global aerosol optical depth validation based on 2 years of coincident Aerosol Robotic Network (AERONET) observations, J. Geophys. Res., 110, D10S04, 10.1029/2004jd004706, 2005.

Kaufman, Y. J., Tanre, D., and Boucher, O.: A satellite view of aerosols in the climate system, Nature, 419, 215-223, 2002.

Krotkov, N. A., et al.: Comparison of TOMS and AVHRR Volcanic Ash Retrievals from the August 1992 Eruption of Mt. Spurr, Geophysical Research Letters, 26, 4, 455-458, 1999.

Liu, Z., Kuehn, R., Vaughan, M., Winker, D., Omar, A., Powell, K., Trepte, C., Hu, Y., and Hostetler, C. : The CALIPSO Cloud And Aerosol Discrimination: Version 3 Algorithm and Test Results, 25th International Laser Radar Conference (ILRC), St. Petersburg, Russia, July 5-9, 2010 S11O-07.

Marenco, F., Johnson, B., Turnbull, K., Newman, S., Haywood, J., Webster, H., and

Ricketts, H.: Airborne lidar observations of the 2010 Eyjafjallajkull volcanic ash plume, Journal of Geophysical Research D: Atmospheres, 116, 2011.

Martins, J. V., Tanré, D., Remer, L., Kaufman, Y., Mattoo, S., and Levy, R.: MODIS cloud screening for remote sensing of aerosols over oceans using spatial variability, Geophysical Research Letters, 29, 4-1 - 4-4, 2002.

Martonchik, J. V., Diner, D. J., Kahn, R. A., Ackerman, T. P., Verstraete, M. M., Pinty, B., and Gordon, H. R.: Techniques for the retrieval of aerosol properties over land and ocean using multiangle imaging, Geoscience and Remote Sensing, IEEE Transactions on, 36, 1212-1227, 1998.

Mason, B. G., Pyle, D. M., and Oppenheimer, C.: The size and frequency of the largest explosive eruptions on Earth, Bulletin of Volcanology, 66, 735-748, 2004.

Mastin, L. G., Guffanti, M., Servranckx, R., Webley, P., Barsotti, S., Dean, K., Durant, A., Ewert, J. W., Neri, A., Rose, W. I., Schneider, D., Siebert, L., Stunder, B., Swanson, G., Tupper, A., Volentik, A., and Waythomas, C. F.: A multidisciplinary effort to assign realistic source parameters to models of volcanic ash-cloud transport and dispersion during eruptions, Journal of Volcanology and Geothermal Research, 186, 10-21, 2009.

Millington, S. C., Saunders, R. W., Francis, P. N., and Webster, H. N.: Simulated volcanic ash imagery: A method to compare NAME ash concentration forecasts with SEVIRI imagery for the Eyjafjallajkull eruption in 2010, Journal of Geophysical Research D: Atmospheres, 117, 2012.

Naeger, A. R., S. A. Christopher, R. Ferrare, and Z. Liu.: A new technique using infrared satellite measurements to improve the accuracy of the CALIPSO cloud-aerosol discrimination method, IEEE Transactions on Geoscience and Remote Sensing, *51*(1), 642-653, 2013.

Patadia, F., Yang, E.-S., and Christopher, S. A.: Does dust change the clear sky top of atmosphere shortwave flux over high surface reflectance regions?, Geophysical Research Letters, 36, L15825, 10.1029/2009gl039092, 2009.

Pavolonis, M. J., Feltz, W. F., Heidinger, A. K., and Gallina, G. M.: A daytime complement to the reverse absorption technique for improved automated detection of volcanic ash, Journal of Atmospheric and Oceanic Technology, 23, 1422-1444, 2006.

Pergola, N., Tramutoli, V., Marchese, F., Scaffidi, I., and Lacava, T.: Improving volcanic ash cloud detection by a robust satellite technique, Remote Sensing of Environment, 90, 1-22, 2004.

Prata, A. J.: Infrared radiative transfer calculations for volcanic ash clouds, Geophysical Research Letters, 16, 1293-1296, 1989.

Prata, A. J., and Kerkmann, J.: Simultaneous retrieval of volcanic ash and SO2 using MSG-SEVIRI measurements, Geophysical Research Letters, 34, 2007.

Prata, F., Bluth, G., Rose, B., Schneider, D., and Tupper, A.: Comments on "Failures in detecting volcanic ash from a satellite-based technique", Remote Sensing of Environment, 78, 341-346, 2001.

Remer, L. A., Kaufman, Y. J., Tanré, D., Mattoo, S., Chu, D. A., Martins, J. V., Li, R.-R., Ichoku, C., Levy, R. C., Kleidman, R. G., Eck, T. F., Vermote, E., and Holben, B. N.: The MODIS Aerosol Algorithm, Products, and Validation, Journal of the Atmospheric Sciences, 62, 947-973, doi:10.1175/JAS3385.1, 2005.

Riggs, G.A., and Hall, D.K.: Snow Mapping with the MODIS Aqua Instrument, 61st Eastern Snow Conference, Portland, Maine, 9-11 June 2004, 81-84.

Saunders, R. W., and Kriebel, K. T.: An improved method for detecting clear sky and cloudy radiances from AVHRR data (North Atlantic), International Journal of Remote Sensing, 9, 123-150, 1988.

Savtchenko, A., Ouzounov, D., Ahmad, S., Acker, J., Leptoukh, G., Koziana, I., and Nickless D.: Terra and Aqua MODIS products available from NASA GES DAAC, Adv. Space Res., 34(4), 710-714, 2004.

Schmetz, J., Pili, P., Tjemkes, S., Just, D., Kerkmann, J., Rota, S., and Ratier, A.: An Introduction to Meteosat Second Generation (MSG), Bulletin of the American Meteorological Society, 83, 977-992, doi:10.1175/1520-0477(2002)083<0977:AITMSG>2.3.CO;2, 2002.

Schumann, U., Weinzierl, B., Reitebuch, O., Schlager, H., Minikin, A., Forster, C., Baumann, R., Sailer, T., Graf, K., Mannstein, H., Voigt, C., Rahm, S., Simmet, R., Scheibe, M., Lichtenstern, M., Stock, P., Rüba, H., Scḧauble, D., Tafferner, A., Rautenhaus, M., Gerz, T., Ziereis, H., Krautstrunk, M., Mallaun, C., Gayet, J. F., Lieke, K., Kandler, K., Ebert, M., Weinbruch, S., Stohl, A., Gasteiger, J., Gro, S., Freudenthaler, V., Wiegner, M., Ansmann, A., Tesche, M., Olafsson, H., and Sturm, K.: Airborne observations of the Eyjafjalla volcano ash cloud over Europe during air space closure in April and May 2010, Atmospheric Chemistry and Physics, 11, 2245-2279, 2011.

Sigmundsson, F., Hreinsdóttir, S., Hooper, A., Árnadóttir, T., Pedersen, R., Roberts, M. J., Óskarsson, N., Auriac, A., Decriem, J., Einarsson, P., Geirsson, H., Hensch, M., Ófeigsson, B. G., Sturkell, E., Sveinbjörnsson, H., and Feigl, K. L.: Intrusion triggering of the 2010 Eyjafjallajökull explosive eruption, Nature, 468, 426-432, 2010.

Stephens, G. L., Vane, D. G., Boain, R. J., Mace, G. G., Sassen, K., Wang, Z., Illingworth, A. J., O'Connor, E. J., Rossow, W. B., Durden, S. L., Miller, S. D., Austin, R. T., Benedetti, A., Mitrescu, C., and CloudSat Science Team, T.: THE CLOUDSAT MISSION AND THE A-TRAIN: : A new dimension to space-based observations of clouds and precipitation, Bulletin of the American Meteorological Society, 83, 1771-1790, doi:10.1175/BAMS-83-12-1771, 2002.

Torres, O., Bhartia, P. K., Herman, J. R., Ahmad, Z., and Gleason, J. .: Derivation of aerosol properties from satellite measurements of backscattered ultraviolet radiation: Theoretical basis, Journal of Geophysical Research D: Atmospheres, 103(D14), 17099-17110, 1998.

Turnbull, K., Johnson, B., Marenco, F., Haywood, J., Minikin, A., Weinzierl, B., Schlager, H., Schumann, U., Leadbetter, S., and Woolley, A.: A case study of observations of volcanic ash from the Eyjafjallajökull eruption: 1. in situ airborne observations, Journal of Geophysical Research D: Atmospheres, 117, 2012.

Vaughan, M. A., Young, S. A., Winker, D. M., Powell, K. A., Omar, A. H., Liu, Z., Hu, Y., and Hostetler, C. A.: Fully automated analysis of space-based lidar data: an overview of the CALIPSO retrieval algorithms and data products, Maspalomas, Gran Canaria, Spain, 2004, 16-30.

Weber, K., Eliasson, J., Vogel, A., Fischer, C., Pohl, T., van Haren, G., Meier, M., Grobéty, B., and Dahmann, D.: Airborne in-situ investigations of the Eyjafjallajökull volcanic ash plume on iceland and over north-western Germany with light aircrafts and optical particle counters, Atmospheric Environment, 48, 9-21, 2012.

Webley, P. W., Steensen, T., Stuefer, M., Grell, G., Freitas, S., and Pavolonis, M.: Analyzing the Eyjafjallajkull 2010 eruption using satellite remote sensing, lidar and WRF-Chem dispersion and tracking model, Journal of Geophysical Research D: Atmospheres, 117, 2012.

Zhang, P., Lu, N. m., Hu, X. q., and Dong, C. h.: Identification and physical retrieval of dust storm using three MODIS thermal IR channels, Global and Planetary Change, 52, 197-206, 2006.

Zhu, L., Liu, J., Liu, C., and Wang, M.: Satellite remote sensing of volcanic ash cloud in complicated meteorological conditions, Science China Earth Sciences, 54, 1789-1795, 2011.

Channel	Center (µm)	Min (µm)	Max (µm)
1	0.635	0.56	0.71
2	0.81	0.74	0.88
3	1.64	1.5	1.78
4	3.9	3.48	4.36
5	6.25	5.35	7.15
6	7.35	6.85	7.85
7	8.7	8.3	9.1
8	9.66	9.38	9.94
9	10.8	9.8	11.8
10	12	11	13
11	13.4	12.4	14.4

Table 1. SEVIRI channels with the center, minimum, and maximum wavelengths where the channels used in the SEVIRI algorithm are highlighted in red.

Tests
Feature Tests
$\lvert 0.6\ \mu m_{CUR} - 0.6\ \mu m_{CLR} \rvert > 1.5\%$
Cloud Tests
BTD 8.7-10.8 > -2 K and BTD 10.8-12.0 > 0 K
10.8 µm < 240 K and BTD 10.8-12.0 > -0.5 K
1.6 µm > 30% and BTD 10.8-12.0 > -0.5 K
BTD 10.8-12.0 > 1.5 K
σT 1.6 µm > 1.5% and BTD 10.8-12.0 > 0 K
|0.6 µmCUR-0.6 µmCLR|> 3.5% and BTD 10.8-12.0 > 0 K
σs 1.6 µm > 2.5% and BTD 10.8-12.0 > 0 K
σs 12.0 µm > 1.5 K and BTD 10.8-12.0 > 0 K

Table 2. Outline of the algorithm applied over land which shows the various thresholds used for the feature tests and cloud tests.

1293